Ceramics International 52 (2026) 5269–5277

Contents lists available at ScienceDirect

Ceramics International

journal homepage: www.elsevier.com/locate/ceramint

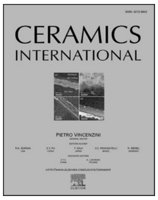

Double magnetization reversal in $Er_3Fe_5O_{12}$ garnet nanocrystals

Novica Paunović [a,*], Zorana Dohčević-Mitrović [a,**], Raneesh Balakrishnan [b], Marko Bošković [c], Marija Perović [c], Bojan Stojadinović [a], Sobi K. Chacko [b,d], Saša Lazović [a], Nandakumar Kalarikkal [e,f,g]

[a] Institute of Physics Belgrade, University of Belgrade, Pregrevica 118, 11080, Belgrade, Serbia
[b] Department of Physics, Catholicate College, Pathanamthitta, Kerala, 689645, India
[c] Vinča Institute of Nuclear Sciences, National Institute of the Republic of Serbia, University of Belgrade, P.O.Box 522, Belgrade, 11351, Serbia
[d] Department of Physics, NSS Hindu College, Changanassery, Kerala, 686 102, India
[e] School of Pure and Applied Physics, Mahatma Gandhi University, Kottayam, Kerala, 686560, India
[f] International and Inter University Centre for Nanoscience and Nanotechnology, Mahatma Gandhi University, Kottayam, Kerala, 686560, India
[g] International Centre for Ultrafast Studies, Mahatma Gandhi University, Kottayam, Kerala, 686560, India

ARTICLE INFO

Keywords:
$Er_3Fe_5O_{12}$ garnet
Rare-earth garnets
Magnetization reversal
Negative magnetization
Magnetization compensation
Magnetization switching

ABSTRACT

$Er_3Fe_5O_{12}$ nanoparticles were synthesized via the sol-gel method, yielding an *Ia3d* garnet structure, as confirmed by XRD, HRTEM, EDX, and Raman spectroscopy. Magnetic measurements showed that the temperature of magnetic compensation is 75 K (T_{comp1}), and that the coercive field exhibits a single peak near T_{comp1}. Above T_{comp1}, the coercive field was found to be proportional to the susceptibility of the Er^{3+} paraprocess. Zero-field-cooled (ZFC) and field-cooled (FC) measurements were performed, including both cooling (FCC) and warming (FCW) cycles. FCC measurements revealed double magnetization reversal, with two compensation temperatures, observed for the first time in $Er_3Fe_5O_{12}$. At T_{comp1}, the magnetization switches from positive to negative, whereas at the lower T_{comp2}, it switches from negative to positive. T_{comp2} depends on the applied field and increases with increasing field, and for fields above 1000 Oe, the magnetization reversal no longer occurs. In contrast, these magnetization reversals are completely absent in the FCW regime. Additionally, $Er_3Fe_5O_{12}$ nanoparticles exhibit magnetization switching, where the magnetization orientation can be reversed by changing only the magnitude of the applied field while keeping its direction fixed. The observed double magnetization reversal is attributed to a strong magnetocrystalline anisotropy opposing the Zeeman-driven realignment of magnetization.

1. Introduction

Magnetization reversal (MR), also known as negative magnetization, is a phenomenon in which the magnetization changes its direction, transitioning from a positive state (aligned with the external field) to a negative state (opposite to the field) within a specific temperature range. The temperature at which the magnetization becomes zero is referred to as the compensation temperature. Such an effect was first predicted by Néel [1] as a phenomenological possibility in certain ferrimagnetic materials. It arises from the different temperature dependencies of magnetization in two antiferromagnetically coupled magnetic sublattices, which result from different molecular fields acting on magnetic ions positioned at two different crystallographic sites. This behavior was later experimentally observed in spinel ferrites [2]. This unusual and intriguing effect has attracted significant attention due to its importance in fundamental physics and its potential applications in magnetic data storage, spin valves, magnetic switches, thermomagnetic switching, bipolar magnetocaloric devices, and advanced spintronic and memory technologies [3–9]. MR has been experimentally reported in various magnetically ordered materials, such as spinels [2,10–13], perovskites [14–17], particularly in orthochromites [18–22] and orthoferrites [8,23,24]. In contrast, it has been reported in a relatively small number of cases for garnets, e.g., Refs. [25–32].

Erbium iron garnet (ErIG) belongs to the rare-earth iron garnet family, a class of ferrimagnetic materials with a cubic garnet structure. These materials are known for their complex magnetic interactions, magnetization compensation effects, and spin reorientation transitions, making them highly relevant for both fundamental research and

---

* Corresponding author.
** Corresponding author.
E-mail addresses: paun@ipb.ac.rs (N. Paunović), zordoh@ipb.ac.rs (Z. Dohčević-Mitrović).

https://doi.org/10.1016/j.ceramint.2025.12.301
Received 29 September 2025; Received in revised form 4 December 2025; Accepted 18 December 2025
Available online 18 December 2025
0272-8842/

spintronic applications. ErIG crystallizes in a cubic garnet structure with space group *Ia3d*, where Er^{3+} ions occupy dodecahedral (24c) sites, Fe^{3+} ions are distributed between octahedral (16a) and tetrahedral (24d) sites, while O^{2-} ions reside at the 96h positions. The Fe^{3+} ions in octahedral and tetrahedral sites form distinct magnetic sublattices that are antiferromagnetically coupled but unequal in magnitude, resulting in a net magnetization that gives rise to the ferrimagnetic behavior of ErIG. The Er^{3+} ions at dodecahedral sites form a separate magnetic sublattice that weakly antiferromagnetically couples to the resultant magnetization of the Fe sublattices. The Curie temperature in iron garnets is largely independent of the rare-earth ion, as it is primarily determined by the strong exchange interaction between the Fe sublattices. For ErIG, as well as other iron garnets, the Curie temperature is approximately 560 K [33,34]. The magnetizations of the Er and Fe sublattices in ErIG exhibit different temperature dependencies, with the Er sublattice dominating at low temperatures and the Fe sublattices dominating at high temperatures. The temperature at which their opposing magnetizations cancel each other, resulting in zero net magnetization, is known as the compensation temperature (T_{comp}), which for ErIG is approximately 80 ± 5 K [35–37]. At high temperatures, ErIG exhibits an easy magnetization axis along [111], while at low temperatures, it undergoes a spin reorientation toward the [100] direction, and also adopts the so-called double-umbrella structure, in which the Er moments on magnetically inequivalent sites form two canted cones around the Fe axis [37]. This complex spin behavior makes ErIG interesting for both fundamental research and potential applications.

In this paper, we synthesized ErIG nanoparticles and characterized them using XRD, HRTEM, EDX, and Raman spectroscopy. We also performed detailed field- and temperature-dependent magnetic measurements. ErIG was found to exhibit a double MR, a phenomenon not previously reported for this material and observed in only a few other garnets [30–32]. We found that the MR effect is present only in FCC measurements, and completely absent in FCW measurements. Such asymmetry has been reported in systems such as chromates [18,21], but never before in garnets. Additionally, magnetization switching was observed, where the direction of magnetization reverses solely due to changes in the magnitude of the applied field, without altering its direction. These results advance knowledge of ErIG properties and play an important role in the broader understanding of MR in garnets.

2. Experimental

ErIG nanoparticles were prepared by the polyvinyl alcohol (PVA)-mediated sol-gel method. For the preparation of the precursor solution, constituent nitrates $Er(NO_3)_3{\cdot}5H_2O$ and $Fe(NO_3)_3{\cdot}9H_2O$ were used (Sigma-Aldrich). Stoichiometric amounts of the precursors were dissolved in deionized water. The chelating agent PVA was added to the solution in a 1:1 M ratio relative to the total content of metal ions, and the mixture was continuously stirred and maintained at 80 °C to ensure homogeneous gel formation. The resulting gel was dried in an oven at 110 °C for 5 h, and then calcined at 800 °C for 3 h to obtain ErIG nanoparticles.

The crystalline structure of nanocrystalline ErIG was characterized by X-ray diffraction (XRD) using a Rigaku MiniFlex diffractometer with a Cu-Kα radiation source. XRD data were collected over a 2θ range of 10°–80°. The Rietveld refinement of the XRD data was performed using the FullProf Suite. Transmission electron microscopy (TEM), high-resolution transmission electron microscopy (HRTEM) images, and selected area electron diffraction (SAED) patterns were acquired using a JEOL JEM-2100 transmission electron microscope operated at 200 kV. Elemental analysis was performed with an Oxford EDX system attached to the TEM. The room-temperature micro-Raman spectrum was measured in backscattering geometry using a Jobin Yvon T64000 triple spectrometer equipped with a liquid nitrogen-cooled CCD detector and an Ar^+/Kr^+ ion laser operating at a wavelength of 514.5 nm as the excitation source. Magnetic measurements were performed using a Quantum Design MPMS XL5 SQUID magnetometer.

3. Results and discussion

ErIG crystallizes in a body-centered cubic crystal structure with space group *Ia3d* (O_h^{10}, No. 230), schematically presented in Fig. 1. The conventional unit cell contains eight formula units, corresponding to 160 atoms in total. In this structure, the Fe ions occupy two distinct sites: octahedral 16a sites (Fe^O) with sixfold oxygen coordination, and tetrahedral 24d sites (Fe^T) with fourfold oxygen coordination, thus the formula unit can also be represented as $Er_3\left[Fe_2^O\right]\left[Fe_3^T\right]O_{12}$. The Er ions are located at the 24c dodecahedral sites, each surrounded by eight oxygen ions, while the oxygen ions reside at the 96h positions. The room-temperature XRD pattern of the ErIG nanocrystalline sample, along with the Rietveld refinement, is shown in Fig. 2. The diffraction peaks correspond to the body-centered cubic crystal structure of ErIG, indexed to the *Ia3d* space group (JCPDS standard pattern 23–0240). The parameters obtained from the refinement are summarized in Table 1. The obtained crystal lattice constant is 12.34 Å, which is close to previously reported values [38]. Using the Scherrer equation, the average crystallite size was estimated to be approximately 43 nm.

The TEM image in Fig. 3(a) shows a loose agglomeration of irregularly shaped nanoparticles. The histogram of the particle size distribution was analyzed and fitted to a log-normal distribution function, yielding an average grain size of 47 nm. The HRTEM image (Fig. 3(b)) shows distinct lattice fringes with an interplanar spacing of 0.276 nm, corresponding to the (420) planes in the ErIG crystal structure, indicating high crystallinity of the nanoparticles. The SAED pattern (Fig. 3(c)) displays multiple bright rings, characteristic of a polycrystalline sample. EDX analysis was performed to investigate the elemental composition of the synthesized sample, and a representative EDX spectrum of the top surface layers of the nanoparticles is shown in Fig. 3(d). Aside from the Cu peak, which originates from the grid used to disperse the nanoparticles for measurement, only peaks corresponding to Er, Fe, and O were detected, with no impurities observed. The quantitative results are summarized in Table 2, indicating that the elemental composition is close to the stoichiometrically expected values.

The crystalline structure and purity of the ErIG sample were further confirmed by the room-temperature Raman spectrum shown in Fig. 4. Factor-group analysis for the body-centered cubic rare-earth garnet structure with space group *Ia3d* predicts 25 Raman-active phonon modes, classified as $3A_{1g}$, $8E_g$, and $14T_{2g}$ [40–43]. The measured Raman spectrum closely matches those of other rare-earth iron garnets, and the symmetry assignments of the prominent Raman modes are indicated in Fig. 4 according to the literature data [42]. The high-frequency modes (>500 cm^{-1}) are attributed to internal vibrations of the tetrahedral and octahedral units [40,41,44]. In the intermediate region (300–500 cm^{-1}), the E_g modes correspond to internal vibrations involving Er, tetrahedral Fe, and oxygen ions, where Er and Fe vibrate either in phase or out of phase. The T_{2g} modes represent a combination of internal and rotational vibrations of the tetrahedral and octahedral units [44]. The low-frequency modes (<300 cm^{-1}) correspond to translational motions of Er^{3+} ions and the tetrahedral and/or octahedral structural units [40,44,45].

Magnetization curves M(H) were measured at various temperatures between 5 and 300 K, and for clarity, only the selected representative curves are shown in Fig. 5(a). The sample exhibits clear ferrimagnetic behavior at 300 K, with a coercive field of 47 Oe and a remanent magnetization of 1.59 emu/g. Superimposed on the ferrimagnetic behavior is a linear component arising from the paraprocess contribution of Er^{3+} ions. The ferrimagnetic component reaches most of its saturation magnetization of 11.6 emu/g in fields around 2 kOe, and at higher fields, the magnetization is dominated by the linear component. In ErIG, the spin arrangement is governed by a complex interplay among three distinct magnetic sublattices, schematically illustrated in the inset

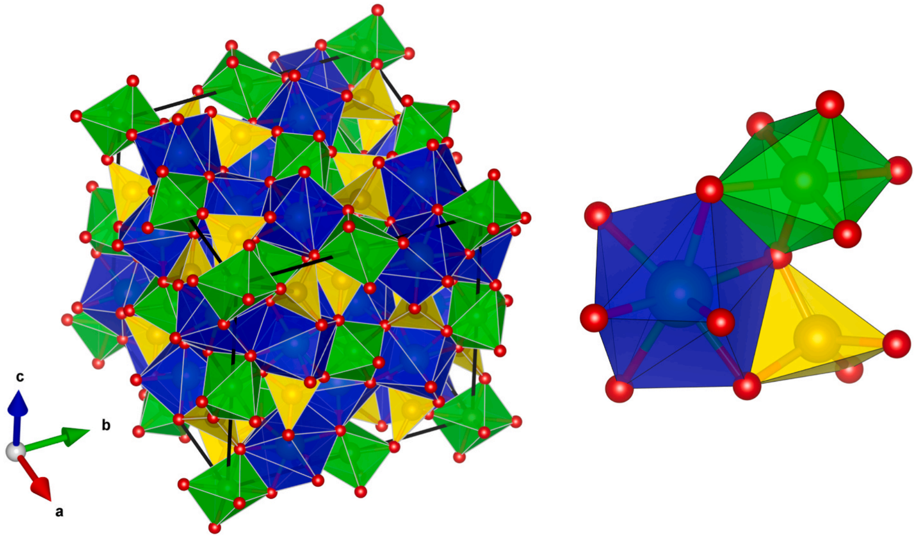

Fig. 1. Crystal Structure of $Er_3Fe_5O_{12}$ ($Er_3\left[Fe_2^O\right]\left[Fe_3^T\right]O_{12}$) erbium iron garnet. The dodecahedral (Er, blue), octahedral (Fe^O, green), and tetrahedral (Fe^T, yellow) local polyhedra environments are shown, with oxygen atoms in red. An enlarged view of one representative set of polyhedra is also included for clarity. The crystal structure was visualized using VESTA 3 [39]. (For interpretation of the references to colour in this figure legend, the reader is referred to the Web version of this article.)

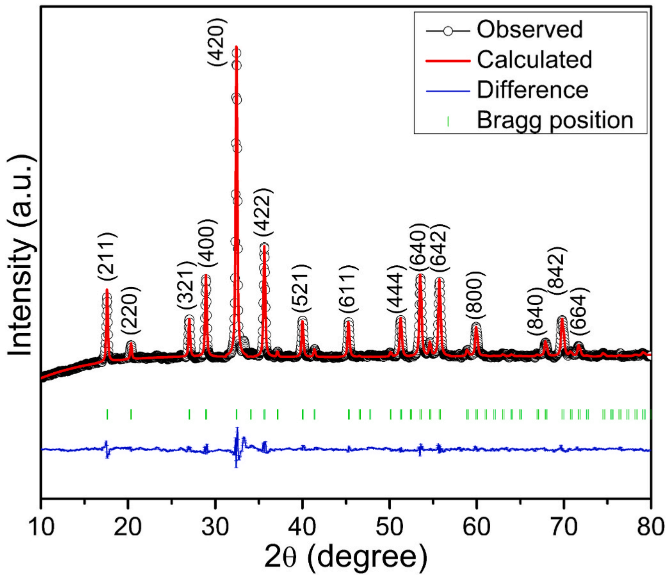

Fig. 2. Rietveld refinement of the XRD pattern of the $Er_3Fe_5O_{12}$ nanocrystalline sample.

Table 1
Crystallographic parameters obtained from the Rietveld refinement of $Er_3Fe_5O_{12}$ at room temperature.

Space group = *Ia3d*, a = 12.3427 Å. χ^2 = 2.856.

Atom	Position	*x*	*y*	*z*
Fe^O	16a	0.000	0.000	0.000
Fe^T	24d	0.375	0.000	0.250
Er	24c	0.125	0.000	0.250
O	96h	−0.0270	0.0568	0.1504

of Fig. 5(b), with magnetizations denoted as M_a, M_d, and M_c. The Fe^{3+} ions occupying octahedral (16a) and tetrahedral (24d) sites are antiferromagnetically coupled due to superexchange interactions mediated by O^{2-} ions. Because the tetrahedral sites host a greater number of Fe^{3+}

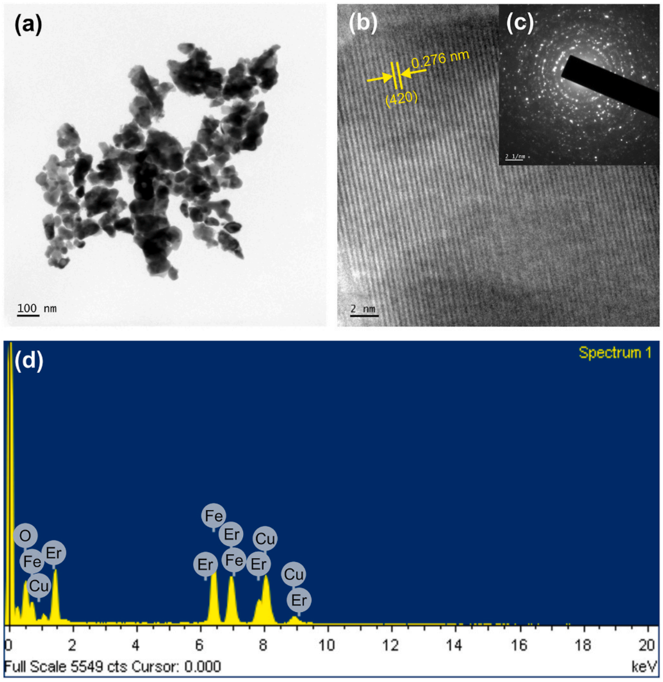

Fig. 3. (a) TEM image, (b) HRTEM image, (c) SAED pattern, and (d) EDX pattern of nanocrystalline $Er_3Fe_5O_{12}$.

Table 2
Elemental composition of the nanocrystalline $Er_3Fe_5O_{12}$ sample obtained from EDX analysis.

Element	Weight % ±5 %	Atomic % ±5 %
O	16.6	55.1
Fe	28.9	27.5
Er	54.5	17.4
Total	100	100

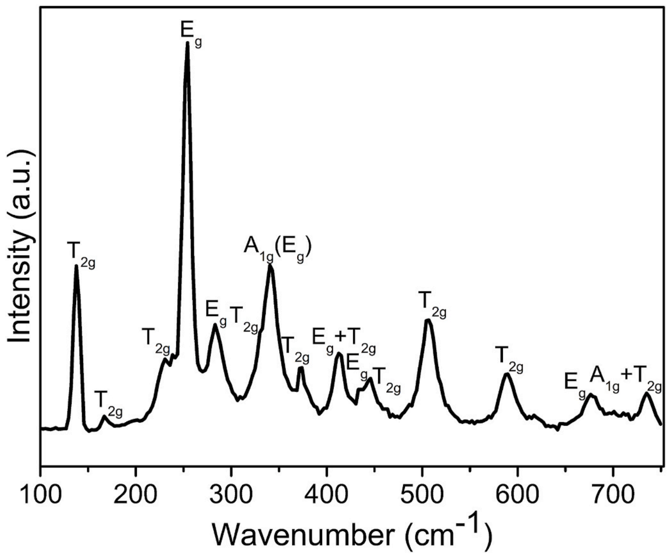

Fig. 4. Room-temperature Raman spectrum of the $Er_3Fe_5O_{12}$ nanocrystalline sample.

ions than the octahedral ones, the magnetization M_d of the tetrahedral sublattice is stronger than the magnetization M_a of the octahedral sublattice, resulting in a net iron sublattice magnetization of $M_d - M_a$. The Er^{3+} ions at the dodecahedral (24c) sites, with magnetization M_c, are antiferromagnetically coupled to the resultant magnetization of the Fe sublattices, leading to a total net moment of $(M_d - M_a) - M_c$. The magnetizations of the Er and Fe sublattices exhibit different temperature dependencies. At low temperatures, the Er sublattice dominates. As the temperature rises, the Er sublattice magnetization decreases more rapidly than that of the Fe sublattices. At the compensation temperature (T_{comp}), the magnetizations of the Er and Fe sublattices cancel each other out, resulting in net zero magnetization. Above T_{comp}, the Fe sublattices dominate the net magnetization of the system. At high temperatures, the Er^{3+} ions exhibit a paramagnetic-like behavior known as the paraprocess, subject to the influence of thermal fluctuations, the external magnetic field, and a weak exchange field produced by the iron sublattices [46–49]. This paraprocess leads to the linear high-field behavior observed in the hysteresis curves at these temperatures (Fig. 5(a)). Fig. 5 (b) shows the temperature dependence of the spontaneous magnetization (M_s), obtained by linear extrapolation of the high-field magnetization to zero field. With decreasing temperature, the spontaneous magnetization decreases and becomes zero at the compensation temperature T_{comp}, below which it increases again. The obtained compensation temperature T_{comp} is approximately 75 K, which is similar to previous findings for ErIG [35–37].

From the linear high-field regions of the hysteresis curves measured at different temperatures, we obtained the susceptibility of the superimposed Er^{3+} paraprocess. The temperature dependence of the inverse susceptibility is shown in Fig. 5(c). It can be seen that this dependence is linear from T_{comp} to room temperature. This linear region was fitted with the Curie-Weiss law (which also applies to paraprocesses [50]), $\chi = C/(T-\theta)$, where C is the Curie constant and θ is the Curie-Weiss temperature. The fit, shown as the red dashed line, yielded a Curie constant of 39.5 emu·K·mol^{-1} Oe^{-1}. The obtained Curie-Weiss temperature in

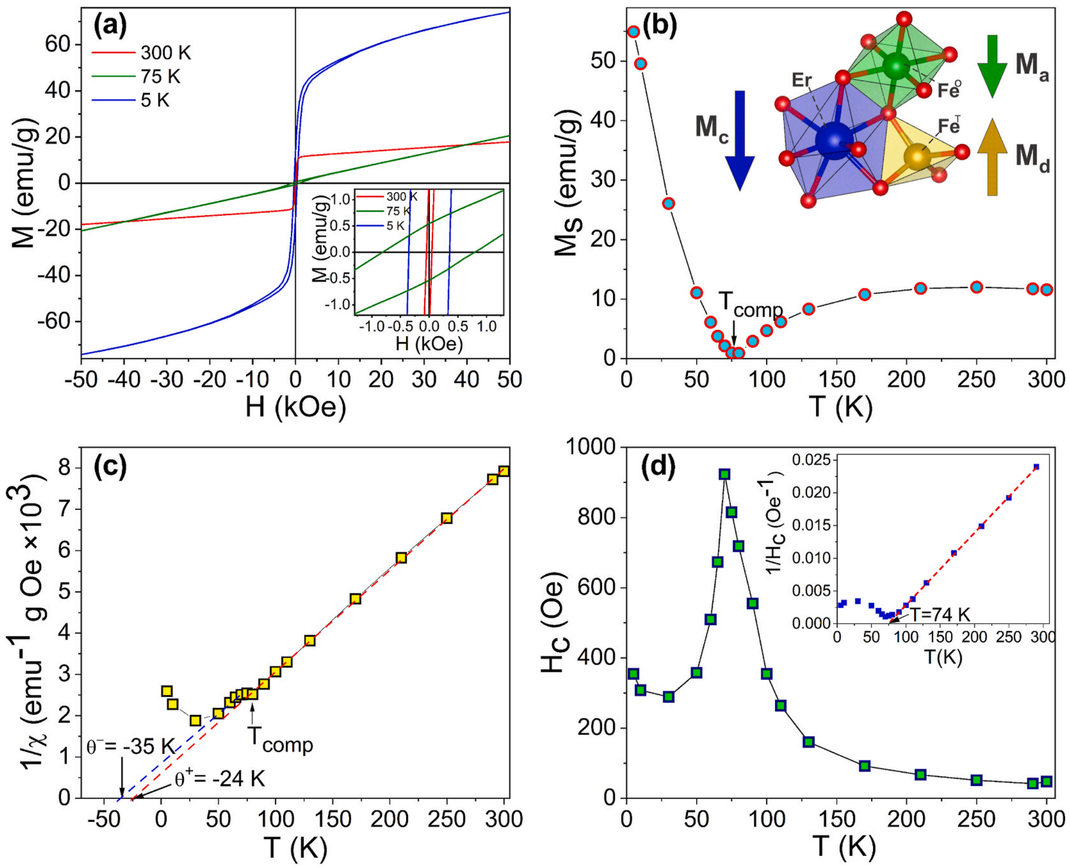

Fig. 5. (a) Magnetization curves M(H) of nanocrystalline $Er_3Fe_5O_{12}$ at selected characteristic temperatures. Inset: a magnified view of the central region of the magnetization curves. (b) Temperature dependence of spontaneous magnetization. Inset: schematic representation of three distinct magnetic sublattices in $Er_3Fe_5O_{12}$. (c) Temperature dependence of the inverse susceptibility, along with Curie–Weiss fits. (d) Temperature dependence of the coercive field. Inset: temperature dependence of its inverse.

this range was $\theta^{+} = -24$ K, indicating a weak antiferromagnetic interaction, and is close to the -19.6 K value reported by Guillot et al. for ErIG single crystal [34,51]. Below T_{comp}, the inverse susceptibility deviates from linear behavior but then enters another short temperature range with linear paraprocess behavior, fitted by the blue dashed line and characterized by a second Curie-Weiss temperature of $\theta^{-} = -35$ K, which is close to the -33 K value reported by Guillot et al. [34,51]. A similar behavior, with two distinct linear paraprocess regions above and below T_{comp} and different Curie-Weiss temperatures, has also been observed in other rare-earth garnets, such as DyIG and HoIG. This has been interpreted as a consequence of differing exchange interactions acting upon rare-earth ions in the respective temperature ranges, with an increasing importance of rare-earth-to-rare-earth exchange interactions at low temperatures [34,51–53].

Fig. 5(d) shows the temperature dependence of the coercive field H_c derived from the hysteresis curves. It can be seen that H_c exhibits a sharp maximum in the vicinity of T_{comp}. This maximum in H_c correlates with the minimum of M_s, indicating that H_c varies approximately inversely with M_s, which is in line with the Stoner–Wohlfarth model [54], where $H_c = 2K/M_s$ and K is the anisotropy constant. Similar behavior has been observed in other rare-earth iron garnets which exhibit either single or double peaks in coercivity near the compensation temperature. In the literature, some confusion remains regarding this behavior. Although the underlying mechanism is generally expected to be the same across all rare-earth iron garnets, reports have shown two coercivity peaks in some compounds [31,46,47,55,56], while others exhibit only a single peak [47,55,57–59]. Moreover, for the same rare-earth iron garnets, certain studies have reported double coercivity peaks, while others have observed only a single peak. For instance, GdIG has been reported to exhibit either a single peak [55,57,59] or double peaks [46,56]. Similarly, HoIG shows a single peak in some studies [55,58] and double peaks in others [31,46,47,55], and DyIG has also been reported with either a single [47,55] or double peak [46]. In the case of ErIG, we observed a single peak in our measurements, while Refs. [46,55] reported double peaks.

Goranskiĭ and Zvezdin [50] proposed a theory based on the Stoner–Wohlfarth model to explain the emergence of a double peak in coercivity near the compensation temperature, which was later extended by Uemura et al. [46]. These models, developed within the molecular-field approximation, assume that near the compensation temperature, the net spontaneous magnetization becomes very small, effectively suppressing magnetostatic interactions. As a result, the system behaves as a single domain, and magnetization reorientation is governed predominantly by coherent rotation under the influence of crystalline anisotropy, rather than by domain wall motion characteristic of multidomain structures. The characteristic double peak in coercivity arises from the interplay between the vanishing net spontaneous magnetization of the iron and rare-earth sublattices at the compensation point, and the paraprocess response of the rare-earth ions, which are influenced by both the external magnetic field and their weak exchange coupling with the iron sublattice. In real materials, however, variations in composition, shape, orientation, compensation temperature, magnetic anisotropy, structural disorder, and other properties across grains and nanoparticles can smear or merge the two peaks, often resulting in a single broadened maximum in the experimental coercivity curve.

The inset in Fig. 5(d) shows the temperature dependence of the inverse coercive field, $1/H_c$. Above the compensation temperature T_{comp}, $1/H_c$ varies linearly with temperature, and a linear extrapolation intersects the temperature axis at 74 K, i.e., near T_{comp}. Since both $1/H_c$ and the inverse paraprocess susceptibility of Er^{3+} ions, $1/\chi$ (Fig. 5(c)), exhibit linear temperature dependence above T_{comp}, this implies that in this range, the coercive field H_c is proportional to susceptibility χ. According to the theories of Goranskiĭ and Zvezdin [50] and Uemura et al. [46], as the temperature moves away from T_{comp} and net magnetization increases, multi-domain structures are expected to form, allowing magnetization reorientation via both domain wall motion and coherent rotation. However, the observed proportionality $H_c \propto \chi$ even well above T_{comp} indicates that coercivity in this range remains governed by the paraprocess of the Er sublattice. This behavior likely reflects the nanostructured nature of the sample, where small particle size suppresses domain wall formation or movement and stabilizes single-domain behavior.

The temperature dependence of the magnetization M(T) was measured under an external magnetic field of 100 Oe using ZFC, FCC, and FCW protocols, as shown in Fig. 6. In the ZFC measurement, the sample was first cooled to 3 K in the absence of a magnetic field, and the magnetization was recorded upon warming under the applied field. Subsequently, the FCC measurement was carried out by cooling the sample from 300 K to 3 K in the presence of the same field, followed by the FCW measurement taken during the warming cycle.

The ZFC curve shows a sharp maximum around 11 K, after which it decreases, reaches zero, and then increases again. Above 11 K, the ZFC curve qualitatively resembles the behavior of the spontaneous magnetization shown in Fig. 5(b), as both are governed by similar underlying dynamics between the Er and Fe sublattices. At low temperatures, the Er sublattice dominates, but its magnetization decreases with increasing temperature more rapidly than that of the Fe sublattice. At a certain temperature, the magnetizations of the two sublattices cancel each other out, and at higher temperatures, the Fe sublattice becomes dominant.

A notable feature in the FCC measurements is the appearance of MR at two compensation temperatures. As can be seen from Fig. 6, with decreasing temperature, the 100 Oe FCC curve exhibits the first MR, crossing zero at $T_{comp1} \approx 75$ K. This temperature corresponds to the T_{comp} determined from the M_s vs. T measurements (Fig. 5(b)), at which the Er and Fe sublattice magnetizations are mutually compensated. Below T_{comp1}, the magnetization becomes negative, i.e., opposite to the direction of the external field. Upon further cooling, the magnetization reaches a maximum negative value, then increases and exhibits the second MR at $T_{comp2} \approx 27$ K, below which it becomes positive again. The FCC curves measured under different applied fields are shown in Fig. 7, with an enlarged view of the region between T_{comp1} and T_{comp2} presented in inset (a). The lower compensation temperature, T_{comp2}, increases with increasing field (inset (b) of Fig. 7), whereas the higher compensation temperature, T_{comp1}, is practically independent of the applied magnetic field. For fields of approximately 1000 Oe and above, T_{comp2} merges with T_{comp1}, and the FCC curve no longer exhibits the MR.

The observed behavior of the FCC curves can be explained as a consequence of competition between the anisotropy energy and Zeeman

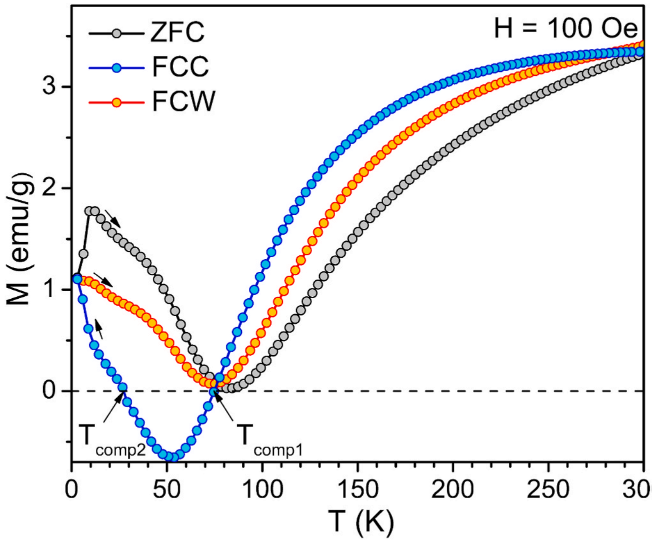

Fig. 6. Temperature-dependent magnetization curves in ZFC, FCC, and FCW measurements at an applied field of 100 Oe.

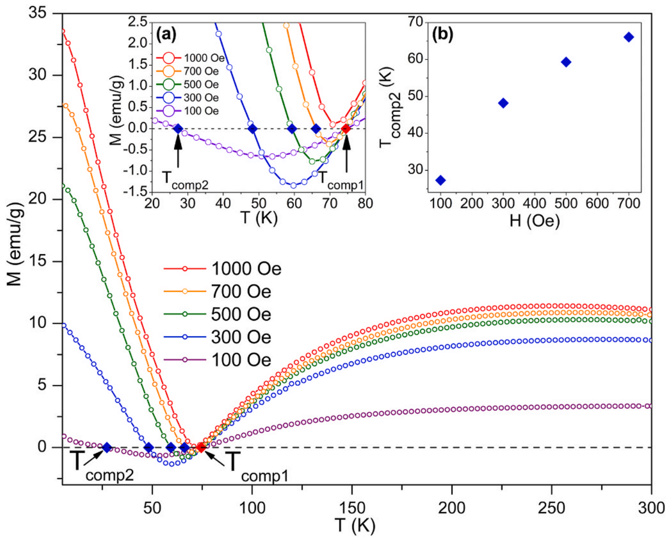

Fig. 7. FCC magnetization curves under various applied fields. Inset (a): enlarged section of the FCC curves in the range between T_{comp1} and T_{comp2}. Inset (b): Variation of T_{comp2} with the applied field.

energy. At high temperatures, above T_{comp1}, the easy axis in ErIG lies along the [111] direction, and the resultant net magnetization is dominated by the Fe sublattices. When an external magnetic field is applied, the net magnetization tends to align with the field direction. The Er and Fe sublattices have antiparallel magnetizations with different temperature dependencies, and at T_{comp1}, their opposing contributions cancel each other. Around T_{comp1}, the easy axis shifts from the [111] to the [100] direction [35,37,60]. With further temperature decrease, the Er sublattice magnetization becomes stronger than that of the Fe sublattices. However, due to the strong magnetocrystalline anisotropy of Er ions, the net magnetization cannot readily reorient along the applied field direction. Instead, it continues to increase in the direction opposite to the applied field, resulting in negative magnetization. Due to the Zeeman energy, this antiparallel orientation of the net magnetization and the field is energetically unfavorable, and below T_{comp1}, as the Er sublattice magnetization becomes increasingly dominant, the net magnetization begins to rotate toward a more favorable parallel alignment with the field. Eventually, the Zeeman energy overcomes the anisotropy barrier, resulting in reorientation of the net magnetization along the direction of the external field, becoming positive again below T_{comp2}. The stronger the applied field, the greater is the Zeeman energy relative to the anisotropy energy, and the increasing magnetization can overcome the anisotropy barrier at higher temperatures, which explains why T_{comp2} shifts to higher temperatures with increasing applied field (Fig. 7). For sufficiently strong fields (~1000 Oe), the Zeeman energy is large enough to rotate the net magnetization, thus preventing the development of negative magnetization. Fig. 8 presents a simplified schematic illustrating only the main features of this evolution. In contrast, the FCW curves do not exhibit negative magnetization at any field. The fact that the FCC starts from a system with the easy axis along the [111] direction, while the FCW starts from a system with the easy axis along the [100] direction, likely plays an important role in the asymmetry between the cooling and warming curves. Related to this, it is also possible that the system exhibits much lower anisotropy when starting from a low temperature and easy axis along the [100] direction, allowing the magnetization to align more readily with the applied field and thereby suppressing the negative magnetization observed in the FCC case.

The MR phenomenon is rare in itself, but MR with two or more compensation temperatures has been reported in an even more limited number of materials, e.g., Refs. [9,11–13,16,18,19,21,31,32], associated with a broad spectrum of different explanatory mechanisms. For instance, in $NdCr_{1-x}Fe_xO_3$, the MR was attributed to the competition between the weak ferromagnetism of Cr^{3+} ions and the paramagnetic moments of Nd^{3+} and Fe^{3+} ions under the effect of a negative internal magnetic field [9]. In YVO_3, the two magnetization reversals were attributed to the competition between single-ion anisotropy and the Dzyaloshinsky–Moriya–driven canting of the antiferromagnetic sublattices [16]. In ErIG, we attribute the double MR to the competition between Zeeman-driven realignment of the magnetization and magnetocrystalline anisotropy. In most materials, the FCW and FCC curves look essentially the same. However, in our ErIG sample, the FCW curve differs markedly from the FCC curve and does not exhibit any MR, remaining positive at all temperatures. Reports that show significantly different behavior between FCC and FCW curves are also relatively rare, e.g., Refs. [18,21,22]. Among garnets, only a few reports have documented the presence of two compensation temperatures [30–32]. However, to the best of our knowledge, no rare-earth garnet compound has been reported to exhibit significantly different behavior between FCW and FCC curves. The presence of spin reorientation certainly plays an important role in this asymmetry. At the same time, spin reorientation is not unique to ErIG, but occurs in other rare-earth garnets as well. However, Er^{3+} has very high anisotropy, particularly at low temperatures, and considering that ErIG has the lowest T_{comp} in this family and that magnetocrystalline anisotropy generally increases with decreasing temperature, and given the importance of anisotropy in the double MR of ErIG, all of this may contribute to the distinct behavior of ErIG relative to other rare-earth garnets.

The appearance of a sharp maximum near 11 K in the ZFC magnetization curve is intriguing. We believe that this feature is related to the different temperature dependencies of the Er sublattice moments in this temperature range. As mentioned earlier, the easy axis shifts from the

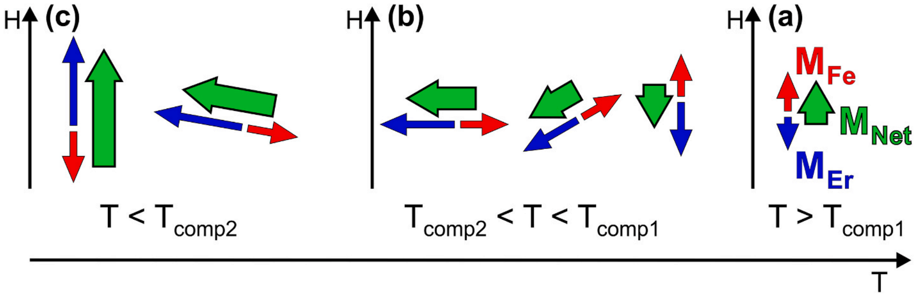

Fig. 8. Schematic illustration of the evolution of magnetic moments in ErIG during FCC, responsible for the observed double magnetization reversal. From right to left, the progression with decreasing temperature is shown. (a) At T > T_{comp1}, the Fe sublattice (red) dominates over the Er sublattice (blue), and the net magnetization (M_{Net}, green) is in the direction of the external magnetic field H. (b) Below T_{comp1}, the Er sublattice magnetization begins to dominate. Due to strong anisotropy, M_{Net} does not reorient in the direction of the field, but remains opposite, producing the observed negative magnetization. With further temperature decrease, as the Zeeman energy associated with the growing M_{Net} increases, M_{Net} gradually rotates toward H. (c) Below T_{comp2}, the net magnetization is again oriented toward H and positive. (For interpretation of the references to colour in this figure legend, the reader is referred to the Web version of this article.)

[111] to the [100] direction around and below T_{comp} [35,37,60]. Moreover, below T_{comp}, ErIG also adopts the so-called double-umbrella structure, in which the Er moments form two conical arrangements around the Fe spin axis, with different canting angles and magnetic moments for the two magnetically inequivalent Er sites (8b and 16e). This complex magnetic structure arises from the interplay of crystal-field anisotropy at the Er sites and Fe–Er superexchange interactions. Such a magnetic structure has been observed in ErIG, as well as in several other rare-earth iron garnets, based on neutron diffraction and Mössbauer spectroscopy studies [37,61–65]. From neutron diffraction measurements, Tcheou et al. found that these magnetically inequivalent Er sites form two cones with angles of 14° and 42° relative to the [111] direction [61]. Hock et al. also conducted neutron diffraction studies on ErIG and performed a detailed refinement of its magnetic and crystallographic structure [37]. They found that ErIG adopts the rhombohedral magnetic space group ($R3c'$) above T_{comp}, transitions to a tetragonal magnetic symmetry ($I4_1/ac'd'$) below 65 K, and that the symmetry of the magnetic structure is possibly further lowered to an orthorhombic configuration below 5 K. They also observed that multiple neutron diffraction reflections, most notably the {200} line, display a pronounced intensity maximum near 12 K, which was attributed to the different temperature dependencies of the erbium moments at the 8b and 16e sites. These findings strongly suggest that the 11 K peak observed in the ZFC magnetization curve essentially reflects the same underlying sublattice dynamics responsible for the 12 K intensity maximum observed in neutron diffraction, and arises from the differing temperature evolutions of the Er sublattice moments at the 8b and 16e sites.

Fig. 9 shows the magnetization switching behavior observed in ErIG. The sample was cooled under a magnetic field of 200 Oe down to 73 K (below T_{comp1}), resulting in a negative magnetization (−0.08 emu/g). The magnetization was then monitored as a function of time. When the field was increased to 1000 Oe without changing its direction, the magnetization switched to a positive value (+0.380 emu/g). This MR is achieved by changing only the magnitude of the field while keeping it in the same direction, which is in stark contrast to conventional magnetic materials, where MR would require reversing the field direction. Repeated field cycling between 200 Oe and 1000 Oe induces fully reversible and stable switching between these two magnetization states. As shown in Fig. 9, the magnetization remains constant at each field level, with no time-dependent relaxation, indicating robust and reproducible field-induced reversal. Similar magnetization switching has been reported in other systems such as chromites [6,7,11,18,19], and is considered an attractive property for potential applications.

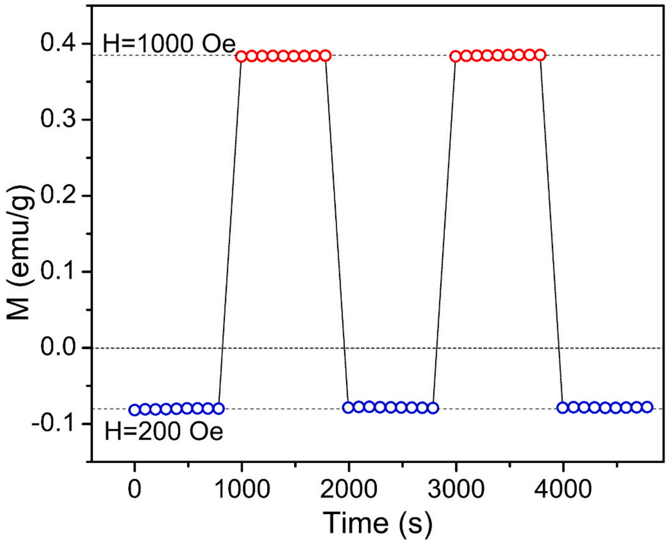

Fig. 9. Magnetization switching in nanocrystalline $Er_3Fe_5O_{12}$ induced by cycling the magnetic field magnitude (200 Oe to 1000 Oe) at 73 K, demonstrating reversible and stable switching under a constant field direction.

4. Conclusions

In summary, $Er_3Fe_5O_{12}$ nanoparticles with the *Ia3d* garnet structure were synthesized via the sol-gel method. M(H) measurements showed that the compensation temperature T_{comp1} is 75 K, and that the coercive field exhibits a single peak near T_{comp1}, indicating that the double coercivity peak often observed in iron garnets is smeared out by variations in grain properties. Two distinct linear paraprocess regions above and below T_{comp1}, each characterized by a different Curie-Weiss temperature, were found, originating from different exchange interactions acting on the rare-earth ions in the respective temperature ranges. Above T_{comp1}, the coercive field was found to be proportional to the paraprocess susceptibility of the Er ions, indicating that coercivity in this temperature range is governed by the paraprocess of the Er sublattice. FCC measurements revealed a double magnetization reversal at two temperatures. The higher T_{comp1} is independent of the applied field, while the lower T_{comp2} increases with increasing field, and for fields above 1000 Oe, the magnetization reversal no longer appears. We interpreted this behavior as a consequence of strong magnetocrystalline anisotropy opposing Zeeman-driven realignment of the net magnetization of the competing Er and Fe sublattices. The magnetization reversals occur only during FCC measurements and are completely absent in the FCW regime. The ZFC curve exhibits a peak at 11 K, which we attributed to the different temperature dependencies of the Er sublattice moments at the 8b and 16e sites. We also observed magnetization switching behavior, in which the magnetization orientation can be reversed by changing only the magnitude of the applied field while keeping its direction fixed. These results reveal interesting and previously unreported aspects of magnetization behavior in ErIG and contribute to the broader understanding of magnetization compensation and reversal processes in rare-earth iron garnets.

CRediT authorship contribution statement

Novica Paunović: Writing – review & editing, Writing – original draft, Visualization, Validation, Project administration, Methodology, Investigation, Funding acquisition, Formal analysis, Data curation, Conceptualization. **Zorana Dohčević-Mitrović:** Writing – review & editing, Writing – original draft, Supervision, Project administration, Methodology, Funding acquisition, Data curation, Conceptualization. **Raneesh Balakrishnan:** Writing – review & editing, Writing – original draft, Visualization, Supervision, Project administration, Methodology, Investigation, Funding acquisition, Formal analysis, Data curation, Conceptualization. **Marko Bošković:** Writing – review & editing, Validation, Resources, Methodology, Investigation, Data curation. **Marija Perović:** Writing – review & editing, Validation, Resources, Methodology, Investigation, Data curation. **Bojan Stojadinović:** Writing – review & editing, Visualization, Methodology, Investigation. **Sobi K. Chacko:** Writing – review & editing, Resources, Methodology, Investigation. **Saša Lazović:** Writing – review & editing, Conceptualization. **Nandakumar Kalarikkal:** Writing – review & editing, Supervision, Project administration, Funding acquisition.

Declaration of competing interest

The authors declare that they have no known competing financial interests or personal relationships that could have appeared to influence the work reported in this paper.

Acknowledgement

The authors gratefully acknowledge funding provided by the Institute of Physics Belgrade, through the grant by the Ministry of Science, Technological Development and Innovation of the Republic of Serbia (Grants No. 451-03-136/2025-03/200024 and 451-03-47/2025-03/200017), and the Serbia-India bilateral project (2022–2024, No. 2). The authors B. R. and N. K. acknowledge the support from the Department of Science and Technology, Govt. of India through India-Serbia Joint S and T project (DST/INT/IND-SERBIA/2022/2). The author N. K. acknowledges SERB: CRG (Grant No. CRG/2021/001506), UGC: Special Assistance Programme (SAP Grant Nos. F.530/12/DRS/2009; F.530/13/DRS II/2016), Scheme for Promotion of Academic and Research Collaboration (SPARC Grant Nos. P930, P1400, P1429, P1460) by MHRD-Govt of India, DST: Nano Mission (Grant No. SR/NM/NS-1420-2014(C)), DST: Fund for Improvement of S&T Infrastructure (FIST Grant No. SR/FST/P SI-143/2009), DAE: UGC-Consortium for Scientific Research (CSR Grant No. UGC-DAE-CSR-KC/CRS/19/RC08/0983/1018), RUSA 2.0 scheme supported by Department of Higher Education, Govt. of India, DAE-Board of Research in Nuclear Sciences (BRNS Grant No. 39/29/2015-BRNS/39009), and DST Promotion of University Research and Scientific Excellence (PURSE Grant No. SR/S9/Z-23/2010/22(C, G)), Government of India programmes for providing facilities for research and development in IIUCNN, MGU.

References

[1] M.L. Néel, Propriétés magnétiques des ferrites; ferrimagnétisme et antiferromagnétisme, Ann. Phys. 12 (3) (1948) 137–198.
[2] E.W. Gorter, J.A. Schulkes, Reversal of spontaneous magnetization as a function of temperature in LiFeCr spinels, Phys. Rev. 90 (3) (1953) 487–488.
[3] A. Kumar, S.M. Yusuf, The phenomenon of negative magnetization and its implications, Phys. Rep. 556 (2015) 1–34.
[4] P. Mandal, A. Sundaresan, C.N.R. Rao, A. Iyo, P.M. Shirage, Y. Tanaka, C. Simon, V. Pralong, O.I. Lebedev, V. Caignaert, B. Raveau, Temperature-induced magnetization reversal in BiFe$_{0.5}$Mn$_{0.5}$O$_3$ synthesized at high pressure, Phys. Rev. B 82 (10) (2010) 100416.
[5] S.M. Yusuf, A. Kumar, J.V. Yakhmi, Temperature- and magnetic-field-controlled magnetic pole reversal in a molecular magnetic compound, Appl. Phys. Lett. 95 (18) (2009).
[6] J. Krishna Murthy, A. Venimadhav, Magnetization reversal phenomena and bipolar switching in La$_{1.9}$Bi$_{0.1}$FeCrO$_6$, Phys. B Condens. Matter 448 (2014) 162–166.
[7] J. Mao, Y. Sui, X. Zhang, Y. Su, X. Wang, Z. Liu, Y. Wang, R. Zhu, Y. Wang, W. Liu, J. Tang, Temperature- and magnetic-field-induced magnetization reversal in perovskite YFe$_{0.5}$Cr$_{0.5}$O$_3$, Appl. Phys. Lett. 98 (19) (2011).
[8] S. Cao, H. Zhao, B. Kang, J. Zhang, W. Ren, Temperature induced spin switching in SmFeO$_3$ single crystal, Sci. Rep. 4 (1) (2014) 5960.
[9] T. Bora, S. Ravi, Sign reversal of magnetization and tunable exchange bias field in NdCr$_{1-x}$Fe$_x$O$_3$ (x=0.05–0.2), J. Magn. Magn Mater. 386 (2015) 85–91.
[10] R. Padam, S. Pandya, S. Ravi, A.K. Nigam, S. Ramakrishnan, A.K. Grover, D. Pal, Magnetic compensation effect and phase reversal of exchange bias field across compensation temperature in multiferroic Co(Cr$_{0.95}$Fe$_{0.05}$)$_2$O$_4$, Appl. Phys. Lett. 102 (11) (2013).
[11] C. Li, T. Yan, G. Zerihun, Q. Fu, R. Zhang, X. Chen, S. Huang, S. Yuan, Magnetization reversal induced by Mn substitution in spinel chromite NiCr$_2$O$_4$, J. Am. Ceram. Soc. 101 (12) (2018) 5571–5577.
[12] H.-g. Zhang, W.-h. Wang, E.-k. Liu, X.-d. Tang, G.-j. Li, H.-w. Zhang, G.-h. Wu, Compensation effect and magnetostriction in CoCr$_{2-x}$Fe$_x$O$_4$, Phys. Status Solidi 250 (7) (2013) 1287–1292.
[13] Y. Qiu, S.S. Zheng, C.L. Li, G.O. Barasa, M.L. Chen, L. Wang, Y.F. Zhao, Y. Lu, Y. S. Luo, Size-dependent compensation effect and negative magnetization in Co (Cr$_{0.9}$Fe$_{0.1}$)$_2$O$_4$ annealed at different temperatures, J. Alloys Compd. 901 (2022) 163692.
[14] J. Mantilla, M. Morales, W. Venceslau, L. Corredor, P.C. Morais, F.F.H. Aragón, S. William da Silva, J.A. Coaquira, Field-driven spin reorientation in SmMnO$_3$ polycrystalline powders, J. Alloys Compd. 845 (2020) 156327.
[15] J. Hemberger, S. Lobina, H.A. Krug von Nidda, N. Tristan, V.Y. Ivanov, A. A. Mukhin, A.M. Balbashov, A. Loidl, Complex interplay of 3d and 4f magnetism in La$_{1-x}$Gd$_x$MnO$_3$, Phys. Rev. B 70 (2) (2004) 024414.
[16] Y. Ren, T.T.M. Palstra, D.I. Khomskii, A.A. Nugroho, A.A. Menovsky, G. A. Sawatzky, Magnetic properties of YVO$_3$ single crystals, Phys. Rev. B 62 (10) (2000) 6577–6586.
[17] A.N. Ulyanov, D.-S. Yang, S.V. Savilov, Negative magnetization, shielding current effect and divalent manganese in CaMn$_{1-x}$Ta$_x$O$_3$ manganites, J. Alloys Compd. 967 (2023) 171686.
[18] K. Yoshii, Magnetization reversal in TmCrO$_3$, Mater. Res. Bull. 47 (11) (2012) 3243–3248.
[19] P. Gupta, P. Poddar, Temperature and magnetic field-assisted switching of magnetization and observation of exchange bias in YbCrO$_3$ nanocrystals, Inorg. Chem. 54 (19) (2015) 9509–9516.
[20] Y. Su, J. Zhang, Z. Feng, L. Li, B. Li, Y. Zhou, Z. Chen, S. Cao, Magnetization reversal and Yb^{3+}/Cr^{3+} spin ordering at low temperature for perovskite YbCrO$_3$ chromites, J. Appl. Phys. 108 (1) (2010).
[21] P. Jain, S. Sharma, R. Baumbach, A.K. Yogi, I. Ishant, M. Majumder, T. Siegrist, M. K. Chattopadhyay, N.P. Lalla, Structural role in temperature-induced magnetization reversal revealed in distorted perovskite Gd$_{1-x}$Y$_x$CrO$_3$, Phys. Rev. B 109 (9) (2024) 094410.
[22] N. Sharma, B.K. Srivastava, A. Krishnamurthy, A.K. Nigam, Hysteresis in magnetization–temperature curves of the orthochromite La$_{0.1}$Gd$_{0.9}$CrO$_3$, J. Alloys Compd. 545 (2012) 50–52.
[23] S.J. Yuan, W. Ren, F. Hong, Y.B. Wang, J.C. Zhang, L. Bellaiche, S.X. Cao, G. Cao, Spin switching and magnetization reversal in single-crystal NdFeO$_3$, Phys. Rev. B 87 (18) (2013) 184405.
[24] T. Bora, S. Ravi, Study of magnetization reversal in LaCr$_{1-x}$Fe$_x$O$_3$ compounds, J. Appl. Phys. 114 (3) (2013) 033906.
[25] B. Lüthi, Anomalous magnetizations in the yttrium gallium iron garnet System and the exchange constant of yttrium iron garnet, Phys. Rev. 148 (2) (1966) 519–521.
[26] Y.G. Chukalkin, V.R. Shtirts, Peculiairities of magnetic properties of the garnet Y$_{2.25}$Gd$_{0.75}$Fe$_5$O$_{12}$ irradiated by fast neutrons, Phys. Status Solidi 173 (2) (1999) 459–465.
[27] I.J. Park, K.U. Kang, C.S. Kim, Temperature-Dependent magnetic properties of bismuth substituted terbium–iron garnets, IEEE Trans. Magn. 42 (10) (2006) 2882–2884.
[28] I.J. Park, C.S. Kim, Structural and magnetic characteristics of bismuth substituted holmium iron garnet, Phys. Status Solidi 244 (12) (2007) 4562–4565.
[29] S. Ravi Aakansha, Investigation of negative magnetization and impedance spectroscopy of Sm-substituted gadolinium iron garnets, Mater. Res. Express 6 (12) (2019) 126113.
[30] C. Li, G.O. Barasa, Y. Qiu, S. Yuan, Magnetocaloric effect and sign reversal of magnetic entropy change across the spin reorientation temperature in R$_3$Fe$_5$O$_{12}$ (R = Gd, Dy), J. Alloys Compd. 820 (2020) 153138.
[31] M. Ghanathe, A. Kumar, I. da Silva, S.M. Yusuf, Magnetic ordering of Ho and its role in the magnetization reversal and coercivity double peaks in the Ho$_3$Fe$_5$O$_{12}$ garnet, J. Magn. Magn Mater. 523 (2021) 167632.
[32] S. Verma, S. Ravi, Analysis of negative magnetization and dielectric studies in holmium substituted samarium iron garnet, Solid State Sci. 139 (2023) 107189.
[33] R. Pauthenet, Spontaneous magnetization of some garnet ferrites and the aluminum substituted garnet ferrites, J. Appl. Phys. 29 (3) (1958) 253–255.
[34] M. Guillot, A. Marchand, F. Tchéou, P. Feldmann, H. Le Gall, Magnetic properties of erbium iron garnet in high magnetic fields up to 150kOe, Z. Phys. B Condens. Matter 44 (1) (1981) 41–52.
[35] M. Guillot, D. Rodic, M. Mitric, Temperature dependencies of the lattice constants and thermal expansion coefficients of Sm$_3$Fe$_5$O$_{12}$ and Er$_3$Fe$_5$O$_{12}$ single crystals, J. Appl. Phys. 73 (10) (1993) 6304–6306.
[36] K. Abdulvakhidov, A. Soldatov, I. Dmitrenko, Z. Li, S. Kallaev, Z. Omarov, The influence of the structural defects on the physical properties of Er$_3$Fe$_5$O$_{12}$ ferrite-garnet, Results Phys. 22 (2021) 103905.
[37] R. Hock, H. Fuess, T. Vogt, M. Bonnet, Low temperature magnetic structure of erbium iron garnet, Z. Phys. B Condens. Matter 82 (2) (1991) 283–294.
[38] J. Zheng, Q. Fu, X. Chen, C. Chakrabarti, P. Wang, H. Yin, C. Li, Y. Qiu, S. Yuan, Colossal dielectric response in erbium iron garnet ceramics, J. Mater. Sci. Mater. Electron. 32 (2020) 290–298.
[39] K. Momma, F. Izumi, VESTA 3 for three-dimensional visualization of crystal, volumetric and morphology data, J. Appl. Crystallogr. 44 (6) (2011) 1272–1276.
[40] G. Mace, G. Schaack, T. Ng, J.A. Koningstein, Optical phonons of terbium-, dysprosium-, and ytterbium-garnet, Zeitschrift für Physik A Hadrons and nuclei 230 (5) (1970) 391–402.
[41] J.P. Hurrell, S.P.S. Porto, I.F. Chang, S.S. Mitra, R.P. Bauman, Optical phonons of yttrium aluminum garnet, Phys. Rev. 173 (3) (1968) 851–856.
[42] J.-J. Song, P.B. Klein, R.L. Wadsack, M. Selders, S. Mroczkowski, R.K. Chang, Raman-active phonons in aluminum, gallium, and iron garnets, J. Opt. Soc. Am. 63 (9) (1973) 1135–1140.
[43] B. Stojadinović, Z. Dohčević-Mitrović, S. Aškrabić, N. Paunović, M.T. Rahul, B. Raneesh, N. Kalarikkal, Spin-phonon interaction in nanocrystalline Dy$_3$Fe$_5$O$_{12}$ probed by Raman spectroscopy: effects of magnetic ordering, J. Sci. Adv. Mater. Devices 8 (3) (2023) 100600.
[44] K. Papagelis, G. Kanellis, S. Ves, G.A. Kourouklis, Lattice dynamical properties of the rare Earth aluminum garnets (RE$_3$Al$_5$O$_{12}$), Phys. Status Solidi 233 (1) (2002) 134–150.
[45] P.B.A. Fechine, E.N. Silva, A.S. de Menezes, J. Derov, J.W. Stewart, A.J. Drehman, I.F. Vasconcelos, A.P. Ayala, L.P. Cardoso, A.S.B. Sombra, Synthesis, structure and vibrational properties of GdIG$_X$:YIG$_{1-X}$ ferrimagnetic ceramic composite, J. Phys. Chem. Solid. 70 (1) (2009) 202–209.
[46] M. Uemura, T.E.S.C.S. Y, S. Nagata, A double peak of the coercive force near the compensation temperature in the rare earth iron garnets, Philos. Mag. 88 (2) (2008) 209–228.
[47] D.T.T. Nguyet, N.P. Duong, T. Satoh, L.N. Anh, T.T. Loan, T.D. Hien, Crystallization and magnetic characterizations of DyIG and HoIG nanopowders fabricated using citrate sol-gel, J. Sci. Adv. Mater. Devices 1 (2) (2016) 193–199.
[48] D.T.T. Nguyet, N.P. Duong, T. Satoh, L.N. Anh, T.D. Hien, Magnetization and coercivity of nanocrystalline gadolinium iron garnet, J. Magn. Magn Mater. 332 (2013) 180–185.
[49] M. Lahoubi, B. Ouladdiaf, Anomalous magnetic reordering in magnetodielectric terbium iron garnet at low temperatures, J. Magn. Magn Mater. 373 (2015) 108–114.
[50] B.P. Goranskiĭ, A.K. Zvezdin, Temperature dependence of the coercive force of ferrimagnets near the compensation temperature, Sov. Phys. - JETP 30 (1970) 299–301.

[51] M. Guillot, A. Marchand, P. Feldmann, H. Le Gall, J.M. Desvignes, Magnetic properties of single crystal erbium iron garnet, J. Appl. Phys. 50 (B3) (1979) 2112–2114.
[52] M. Guillot, P. Feldmann, H.L. Gall, M. Fadly, Molecular field coefficients of terbium, dysprosium and holmium iron garnets, IEEE Trans. Magn. 14 (5) (1978) 909–911.
[53] M. Fadly, P. Feldmann, H.L. Gall, M. Guillot, H. Makram, Magnetooptical coefficients of Ho3+ ions induced by electric and magnetic dipole transitions in single crystal HoIG, IEEE Trans. Magn. 14 (5) (1978) 448–450.
[54] E.C. Stoner, E.P. Wohlfarth, A mechanism of magnetic hysteresis in heterogeneous alloys, Philos. Trans. R. Soc. Lond., Ser. A Math. Phys. Sci. 240 (826) (1948) 599–642.
[55] J. Hanton, Intrinsic coercive force of rare earth iron garnets near the compensation temperature, IEEE Trans. Magn. 3 (3) (1967) 505–509.
[56] K.P. Belov, Rare-earth magnetic materials, Sov. Phys. Usp. 15 (1) (1972) 130.
[57] P. Coeure, J.C. Gay, J. Carcey, Thermomagnetic properties of fine-grain polycrystalline GdIG, IEEE Trans. Magn. 7 (3) (1971) 397–401.
[58] A.M. Kalashnikova, V.V. Pavlov, A.V. Kimel, A. Kirilyuk, T. Rasing, R.V. Pisarev, Magneto-optical study of holmium iron garnet $Ho_3Fe_5O_{12}$, Low Temp. Phys. 38 (9) (2012) 863–869.
[59] W. Doyle, G. Goldberg, W. Flannery, Thermomagnetic writing in GdIG, IEEE Trans. Magn. 6 (3) (1970) 548–553.
[60] Z.M. Stadnik, G.H.M. Calis, H.V. Lipko, Spin reorientation in erbium iron garnet, Solid State Commun. 38 (1981) 719–722.
[61] F. Tcheou, E.F. Bertaut, H. Fuess, II — neutron diffraction study of some rare earth iron garnets RIG (R = Dy, Er, Yb, Tm) at low temperatures, Solid State Commun. 8 (21) (1970) 1751–1758.
[62] S.J. Pickart, H.A. Alperin, A.E. Clark, Rare-Earth sublattice canting in DyIG, ErIG, and YbIG, J. Appl. Phys. 41 (3) (1970) 1192–1193.
[63] F. Sayetat, Huge magnetostriction in $Tb_3Fe_5O_{12}$, $Dy_3Fe_5O_{12}$, $Ho_3Fe_5O_{12}$, $Er_3Fe_5O_{12}$ garnets, J. Magn. Magn Mater. 58 (3) (1986) 334–346.
[64] H. Young Jun, K. Jun Sig, S. In-Bo, K. Chul Sung, Spin rotation at compensation point studies of $Tb_3Fe_5O_{12}$ by Mössbauer spectroscopy, IEEE Trans. Magn. 40 (4) (2004) 2808–2810.
[65] M. Lahoubi, M. Guillot, A. Marchand, F. Tcheou, E. Roudault, Double umbrella structure in terbium iron garnet, IEEE Trans. Magn. 20 (5) (1984) 1518–1520.